https://doi.org/10.1016/j.solmat.2021.111519 **This is the Pre-Published Version.**

Enhanced spectral modulation of Cs_xWO_3 nanocrystals through anionic doping for energy-efficient glazing

***Boxu Shen*[1]*, *Yuanhao Wang*[2,]*, *Lin Lu*[1], *Hongxing Yang*[1]**

1. Renewable Energy Research Group (RERG), Department of Building Services Engineering, The Hong Kong Polytechnic University, Kowloon, Hong Kong

2. SUSTech Engineering Innovation Center, School of Environmental Science and Engineering, Southern University of Science and Technology, Shenzhen, Guangdong 518055, China

*Corresponding author: Boxu Shen; Yuanhao Wang

E-mail addresses: boxushen.shen@connect.polyu.hk (B. Shen);

yuanhaowang@yahoo.com, wangyh2020@mail.sustech.edu.cn (Y. Wang)

Abstract

Spectrally selective materials have been widely used to shield near-infrared radiation for energy-efficient windows in the region with cooling-demand climate. Cs_xWO_3 nanocrystals which exhibit localized surface plasmon resonance (LSPR) and small polaron transfer in wavelength of the near-infrared radiation have attracted great attention to fabricate the spectrally selective coating. The enhancement of its optical performance remains a challenge in the field of doped transition-metal oxide nanocrystals. Herein, F-doped Cs_xWO_3 nanocrystals were successfully prepared with the highest reported absorption coefficient, which demonstrated stronger absorption performance than the Cs_xWO_3 nanocrystals without F doping. The introduction of fluorine into the crystal structure as a cation dopant can enhance the free carrier density of the nanocrystals, which leads to a higher absorption coefficient. The absorption coefficient variation of LSPR and small polaron transfer of F-doped Cs_xWO_3 nanocrystals was explained by the free carrier density and carrier mobility. This substitutional doping strategy allows Cs_xWO_3 nanocrystals to become spectrally tunable within the wavelength of near-infrared radiation. When the F/W molar ratio was 0.4, the free carrier density reached 9.25×10^{14} cm^{-3}. The spectrally selective coating prepared by F-doped Cs_xWO_3 nanocrystals exhibited superior spectral selectivity with T_{Vis}, T_{NIR}, T_{lum}, and T_{sol} of 67.21 %, 11.85 %, 72.76 % and 49.01 %, respectively. This substitutional doping strategy provides promising potential to improve the spectral modulation of Cs_xWO_3 nanocrystals for the practical application of energy-saving windows.

Keywords: F-doped Cs_xWO_3 nanocrystals, energy-efficient windows, absorption coefficient, free carrier density, carrier mobility

1. Introduction

Building energy consumption accounts for approximately 40% of total energy consumption in western countries. [1, 2]. Heating, ventilation, and air conditioning (HVAC) systems make up practically half of the energy used in building [3]. Every year, air-conditionings and fans consume great amounts of electricity to keep building with comfortably indoor temperature [4]. Notably, the buildings in Hong Kong with cooling-demand climate consumed 5.06×10^4 TJ for indoor cooling throughout 2018 [5]. Sunlight passing through windows is the primary source of heat gain in buildings [6-8]. Glazing materials, as the most common component of windows, are widely used in modern buildings to provide daylight and external sight to occupants. Typically, window glazing refers to soda-lime glass, which is composed of silica, sodium oxide, lime, and a small amount of other addition agent via the floating technique. It is established that the solar energy consists of three sorts of radiation, ultraviolet, visible light and near-infrared radiation. Among them, near-infrared light is invisible radiation, accounting for 50% of the total energy from the solar radiation [9, 10].

The visible and near-infrared light transmittance of clear soda-lime glass at 4 mm thickness is around 80 % to 90 % [11], revealing that the ordinary glass lacks the spectral selectivity. Accordingly, it is necessary to develop functional coatings for spectral selectivity, which can not only shield most of the near-infrared radiation, but also maintain a high visible transmittance. This type of spectrally selective coating can inhibit the increase of indoor temperature, finally reducing the electricity consumed by air-conditioning and the emission of greenhouse gas.

Energy-efficient glazing is typically created by applying a light layer made of spectrally selective materials to the glass surface, which can alter how the glass interacts with sunlight [12]. In recent years, spectrally selective materials with superior spectral selectivity have drawn great attention for energy-efficient windows [13-15]. The band gap of tungsten trioxide is 2.62 eV, which hardly shields the near-infrared radiation. However, alkali ions can be doped into the crystal structure of WO_3 to form hexagonal tungsten bronze. Tungsten bronze (M_xWO_3, where M = Na, K, Rb and Cs) is the vital component of the transparent conducive oxides with superior spectral selectivity [4, 16-18]. In particular, the cesium tungsten bronze (Cs_xWO_3) has been extensively studied as the promising candidate for spectral selectivity. The effect of localized surface plasmon resonance (LSPR) and small polaron transfer is responsible for Cs_xWO_3's near-infrared shielding performance. Small polaron transfer mainly absorbs near-infrared radiation with wavelengths ranging from 780 nm to 1100 nm, whereas LSPR of Cs-HTB nanoparticles mainly absorbs NIR radiation with wavelengths ranging from 1100 nm to 2500 nm.. The LSPR effect is prompted by the creation of free charge carriers (free electrons discussed here), which collectively oscillates with incident radiation near the oscillation frequency of the free electrons [19-23]. The effect can result in selective photon absorption and the enhancement of local electromagnetic fields around nanocrystals. The small polarons absorb near-infrared radiation through electron hopping between two neighboring nonequivalent tungsten and the hopping electrons are derived from Cs^+ ions. However, the optical performance of Cs_xWO_3 still requires further improvement from the viewpoint of practical application.

During the last decades, fluorine has been widely introduced into the lattice to enhance the optical property in transparent conducive oxides (TCOs). Generally, the doped fluorine atoms substitute the oxygen sites to form F-doped CdO [24-26], F-doped In_2O_3 [27] and F-doped SnO_2 [28, 29]. In theory, fluorine doping is of the following advantages. Firstly, the radius of F is a little smaller than that of O and F demonstrates higher electronegative than O, so the substitutional process of O by F can easily arise. Moreover, it has been reported that the some doped ions in the lattice acted as a scattering center which limited the highest concentration of free carrier density, but F atoms appear as electron donors as it has one more valence electron than an O atom. Furthermore, compared with cationic substitution doping, the scattering level and decrease of carrier mobility of free electrons can be minimized by anionic F doping. As a result, it is expected that F doping will improve the near-infrared shielding performance of Cs_xWO_3 nanocrystals. To our knowledge, there has yet to be a report on the facile synthesis of F-doped Cs_xWO_3.

In this work, we report for the first time that F-doped Cs_xWO_3 nanocrystals have been successfully synthesized by controllable one-pot method for the application of energy-efficient windows, which expands the spectral tunability of LSPR and small polaron transfer. The effects of F doping on the phase composition, valence state distribution of W, optical properties and microstructure of the as-prepared products have been investigated. Besides, the detailed mechanism for enhancing the near-infrared shielding performance and the effects of charge carrier density and free carrier mobility on LSPR and small polaron transfer have been discussed. The introduction of F doping breaks through the limited tunability of LSPR and small polaron transfer in Cs_xWO_3 nanocrystals. In addition, this doping strategy provides a promising way to regulate the free carrier density and enhance the near-infrared shielding performance in some related nanocrystal systems.

2. Experimental study

2.1 Materials

The following reagents are of analytical grade and utilized as received without further treatment. Ammonium metatungstate hydrate (AMT, $(NH_4)_6H_2W_{12}O_{40}\cdot aH_2O$), cesium fluoride (CsF), tartaric acid (TA, $C_4H_6O_6$), deionized water (H_2O), anhydrous ethanol (C_2H_5OH) and polyvinyl alcohol (PVA) were purchased from Macklin.

2.2 Synthesis of F-doped Cs_xWO_3 nanocrystals

The F-doped Cs_xWO_3 nanocrystals were prepared by controllable one-pot method using CsF as Cs and F source. First, certain quantity of AMT was putted into the ethanol with 1mol/L tartaric acid , then CsF were introduced into the solution of AMT with the Cs/W molar ratio of 0.2, 0.4, 0.6, 0.8. The total volume of the mixed solution was 70 ml. The solution was then transferred to a Teflon-lined autoclave with a 200 ml interval volume, followed by liquid phase reaction in a drying oven at 240 ℃ for 24 hours. The blue products were centrifuged and rinsed three times with anhydrous ethanol and finally dried at 60 ℃ in vacuum. The F-doped Cs_xWO_3 nanocrystals synthesized with the F/W molar ratio of 0.2, 0.4, 0.6, 0.8 were labeled as 0.2-FCWO, 0.4-FCWO, 0.6-FCWO and 0.8-FCWO, respectively. The nanocrystals prepared with Cs/W molar ratio of 0.33 but without F doping were marked as CWO using Cs_2CO_3 as Cs source.

2.3 Fabrication of F-doped Cs_xWO_3 /PVA composite film

The dispersion of the F-doped Cs_xWO_3 was obtained by a simple blending process. PVA powder was applied as the film-formation additive. Typical fabrication procedures of the spectrally selective coating were carried out in the following way. Initially, 4 g PVA powder was melted in deionized water in a water bath at 85 °C to form a homogeneous PVA solution. The as-synthesized nanocrystals were then blended with the above PVA solution for 4 hours using vigorous stirring. The dispersion obtained was then deposited on the glass surface to form the spectrally selective coating.

2.4 Characterization

The phase components of the F-doped Cs_xWO_3 nanocrystals were determined by X-ray diffraction (XRD) technique with Cu Kα radiation. Transmission electron microscopy (TEM) with an energy dispersive spectrum (EDS) attachment was used to examine the microstructure of the nanocrystals. X-ray photoelectron spectroscopy (XPS) was used to investigate the chemical components and binding energies of W 4f. Inductively coupled plasma optical emission spectrometry (ICP-OES) was used to determine the elemental compositions of the nanocrystals in bulk, and the nanocrystals for ICP-OES measurements were digested with concentrated nitric acid and diluted with deionized water. The Hall effect measurements were carried out on LakeShore HL5500 and performed on pellets (10 mm diameter) made by pushing the obtained powders under a pressure of 40 MPa. The absorbance spectra of the as-synthesized nanocrystals were performed on a spectrophotometer (UH 4150) equipped with a cuvette of 0.5 mm pathlength. The optical properties of F-doped Cs_xWO_3 /PVA composite film were measured by UH 4150 equipped with an integrating sphere.

3. Results and discussion

Fig. 1 illustrates the XRD patterns of CWO, 0.2-FCWO, 0.4-FCWO, 0.6-FCWO and 0.8-FCWO and their high-resolution patterns corresponding to crystal plane (102) and (200). As shown in Fig. 1a, when the molar ratio of F/W reached 0.2 and 0.4, a pure hexagonal Cs_xWO_3 phase was obtained without impurity peaks. 0.4-FCWO nanocrystals have better crystallinity than 0.2-FCWO, which indicates that the increase of F/W molar ratio is conducive to the crystallization of as-synthesized nanocrystals to some extent. As for 0.6-FCWO and 0.8-FCWO, impurity peaks appeared, indicating that other phase component has been formed in the nanocrystals besides dominant hexagonal $Cs_{0.33}WO_3$ phase. The peak intensity ratio of crystal plane (002) relative to crystal plane (102) presents an increasing trend with the increase of F/W molar ratio, which means that the preferential growth of the nanocrystals is along the *c*-axes. As shown in Fig. 1b, the (200) plane diffraction peak of 0.4-FCWO slightly shifted to a higher angle, suggesting that the (200) plane spacing becomes smaller. This can be explained according to the Bragg equation as follows:

$$2d\sin\theta = n\lambda \quad (1)$$

where d indicates the crystal interplanar spacing, θ represents the incident angle, λ implies the wavelength of the incident light, n denotes the reflection order. Since $n\lambda$ is a fixed value, the increase of θ suggests the decrease of the crystal interplanar spacing.

The chemical composition and W valence state were determined by XPS measurement. Fig. 2a shows the survey spectra of 0.2-FCWO, 0.4-FCWO, 0.6-FCWO and 0.8-FCWO. All the spectra confirm the presence of Cs, F, W and O elements. As illustrated in Fig. 2b, the difference of F 1s characteristic peak position suggests that the F ions chemical environment in 0.2-FCWO, 0.4-FCWO, 0.6-FCWO and 0.8-FCWO changes with the different F/W molar ratio. Doped F ions are surrounded by O atoms with a certain degree of electronegativity in the crystal lattice. More F ions enter into the lattice and thus its characteristic peak position moves to the higher binding energy direction.

Fig. 3a-e display the W 4f core-level spectra of CWO, 0.2-FCWO, 0.4-FCWO, 0.6-FCWO and 0.8-FCWO. Two spin-orbital peaks, W 4f 5/2 and W 4f 7/2, can be fitted to the W 4f curve. W^{5+} and W^{6+} are responsible for the spin-orbital peaks at 34.2 eV/ 36.7 eV and 35.8 eV/37.9 eV. As shown in Fig. 3f, the content of W^{5+} in 0.4-FCWO is the largest, accounting for 31 % of total W atoms. This indicates that the increase of W^{5+} generation is caused by more Cs and F ions insertion, which plays a significant impact on improving the NIR shielding performance based on LSPR [30]. However, when F/W molar was higher than 0.4, the content of W^{5+} decreased to 23 % and 22 % for 0.6-FCWO and 0.8-FCWO, respectively.

To further examine the effect of F doping on the chemical composition of the as-prepared samples, the molar ratios of Cs/W and F/W in the samples were measured by XPS. The doping ratio of F/W were 0.2, 0.4, 0.6 and 0.8, respectively. As listed in Table 1, the Cs/W molar ratio of the doped samples firstly presented an increasing tend with the increase of F doping. When the doping ratio of F/W reached 0.4, the actual Cs/W content attained maximum value of 0.30, which was close to theoretical Cs/W value of 0.33. Meanwhile, the measured F/W content increased to 0.21. Proceeding to increase the F doping level, the Cs/W content demonstrated a decreasing trend and reached 0.26 when the doping ratio of F/W was 0.8. The F/W content in the as-prepared sample presented a small increasing extent with the increase of Li doping from 0.4 molar ratio. As for 0.4-FCWO, it can be seen that F/W content is 0.21 with the measured Cs/W content of 0.30 which is close to the theoretical value of 0.33. With the increase of F ions in the precursor, the small F ions tend to substitute the sites which are occupied by oxygen during the solvothermal reaction process.

Although the F/W content presented an increasing trend and attained 0.24 for 0.8-FCWO, the Cs/W molar ratio showed a decreasing tendency from 0.4-FCWO and reached 0.26 for 0.8-FCWO, which is not conducive to the crystalline stability and its optical performance.

The Beer-Lambert Law can be described as following eq (2):

$$A = \frac{N\sigma L}{\log(10)} \quad (2)$$

Where A represents the measured absorbance of the dilute nanocrystal dispersion and is expressed in log (10) scale, N indicates the number density of the nanocrystals (M, mol/L), and L (mm) stands for path length through the cuvette. Thus, the absorption coefficient σ (M^{-1} mm^{-1}) of the nanocrystals can be calculated by the above equation using the measured absorbance of the dispersion with known molar concentration and the path length.

To examine the effect of various F doping concentration on the absorption coefficient of the as-prepared nanocrystals, the absorbance of the dilute dispersion containing the as-prepared nanocrystals was measured. Fig. 4 presents the calculated absorption coefficient spectra of all as-synthesized nanocrystals across a set of F doping concentration. With the increase of the dopant concentration, a significant increase of the absorption coefficient can be observed. As shown in Fig. 4, the absorption coefficient spectrum of 0.4-FCWO presents the best absorption potential of all the samples. However, for the samples with the F/W molar ratio of higher than 0.4, the absorption coefficient illustrated a slightly decreasing trend. The results indicate that there must be changes in the optical parameters of the nanocrystals, which is discussed in detail in the following content.

According to the above results, the spectrally selective mechanism of F-doped Cs_xWO_3 nanocrystals is presented in Fig. 5. The near-infrared (NIR) absorption of Cs-HTB nanoparticles is ascribed to LSPR and the small polaron transfer. LSPR of Cs-HTB nanoparticles mostly absorbs

NIR radiation ranging from 1100nm to 2500nm. LSPR is prompted from the free electrons in the conduction band when the incoming radiation is close to the oscillation frequency of the free electrons. As shown in Fig. 5a, a simplified model is presented based on Drude-Lorentz assumptions [31]. The free electrons contributed by the doped alkali ions oscillate in phase with the corresponding electric field component of the sunlight, which results in the spectral selectivity. Moreover, small polaron transfer mainly absorbs the 780-1100nm NIR radiation and consists of two processes shown in Fig. 5b. When surplus electrons polarize their ambient lattice, polarons are formed and defined as the composite of lattice distortion and accompanying free electrons. The polarons absorb NIR light by hopping between two adjacent nonequivalent W ions. The polaron transition process is as follows:

Process I: $h\nu + W^{5+}(a) + W^{6+}(b) \rightarrow W^{6+}(a) + W^{5+}(b) + E_{phonon}$

where E_{phonon} represents single phonon energy.

The electrons transferred between two adjacent nonequivalent W ions are regarded as originating from the doped alkali ions [30]. Besides, there are some electrons in localized states lower than the conduction band of nanoparticles. As shown in Process II, the electrons in localized states would transfer from localized state to conduction band led by absorbing suitable NIR energy. Thus, the majority near-infrared radiation of the sunlight can be effectively shielded by the spectrally selective coating prepared by F-doped Cs_xWO_3 nanocrystals through the above mechanism.

The potential efficiency of creating intense localized electric fields can be evaluated through a performance index originated from the LSPR response termed the Quality factor (Q-factor), which is settled as the ratio of the LSPR peak energy to its full width at half-maximum (FWHM). It is found that the LSPR peak energy is mainly decided by LSPR frequency of the nanocrystals, whilst the FWHM signifies the degree of electron scattering. When impurities are doped into the crystal lattice, a compromise is reached because the dopants create free electrons while also acting as electron scattering centers (increasing FWHM). As a result, balancing the two impacts and raising the Q-factor are critical.A high Q-factor indicates greater near-field improvement, extended plasmon lifespan and lower electronic damping. The LSPR frequency ω_{LSPR} can be depicted by eq (3):

$$\omega_{\mathrm{LSPR}} = \sqrt{\frac{\omega_{\mathrm{p}}^2}{(\varepsilon_\infty + 2\varepsilon_{\mathrm{m}})} - \Gamma^2} \quad (3)$$

where ε_∞ indicates the high-frequency dielectric constant of the material, ε_{m} suggests the dielectric constant of the medium surrounding the nanocrystals and Γ represents the damping constant. As ε_∞ is a distinctive feature that cannot vary with the increase of doping and ε_{m} is determined by the surrounding media. It can be obtained that the variables with a significant impact on the LSPR frequency are the damping constant Γ and the bulk plasma frequency ω_{P} which is described as eq (4):

$$\omega_{\mathrm{p}}^2 = \frac{ne^2}{\varepsilon_0 m^*} \quad (4)$$

where n represents the free carrier density, e indicates the electronic charge, ε_0 presents the permittivity and m^* is the effective mass of the electron. As e and ε_0 are constants for a certain kind of nanocrystals, the spectral selectivity of LSPR depends on n and Γ. In extrinsically doped nanocrystals, the electrostatic interactions between the dopant ions and the electrons can significantly affect scattering level, but Drude model does not premeditate the effect of dopant ions scattering, which provides inevitable scattering in doped nanocrystals. Consequently, an extended Drude model was presented where the damping constant Γ is displaced using a frequency-dependent $\Gamma(\omega)$ by the following empirical eq (5) to describe the scattering degree.

$$\Gamma(\omega) = \Gamma_{\mathrm{L}} - \frac{\Gamma_{\mathrm{L}} - \Gamma_{\mathrm{H}}}{\pi}\left[\tan^{-1}\left(\frac{\omega - \Gamma_{\mathrm{X}}}{\Gamma_{\mathrm{W}}}\right) + \frac{\pi}{2}\right] \quad (5)$$

where Γ_L and Γ_H represent the low-frequency and high-frequency damping constants, respectively. Γ_X indicates the crossover frequency ranging from the low to high frequency domain. Γ_W denotes the width of the crossover region. Thus, it is found that Γ_L qualitatively indicates the scattering extent of dopants ions. To achieve the reductant scattering extent, Γ_L should be minimized as much as possible. It was reported that the electrostatic potential at low frequencies Γ_L would be tantamount to the carriers motion property under the effect of DC electric field [32]. It is noted that carrier mobility under DC electric field is no frequency-dependence. Consequently, $\Gamma_{(0)}$ can be utilized to describe the scattering extent of dopant ions using eq (6):

$$\mu_{\mathrm{opt}} = \frac{e}{m^{*}\Gamma_{(0)}} \quad (6)$$

It can be seen that carrier mobility μ_{opt} plays a significant effect on FWHM and further determine LSPR response. In addition, the electrons transferred between two adjacent nonequivalent W ions are provided by dopant ions, so free carrier density also exerts influence on small polaron transfer. Thus, the effect of free carrier density and carrier mobility on the optical performance should be further studied.

To compare the electrical properties, the hall-effect measurements were conducted to further explain the optical performance of doped nanocrystals. As shown in Table 2, it can be observed that F doping plays a considerable impact on the free carrier density and carrier mobility. When the concentration of F doping increased, the carrier mobility of the corresponding sample illustrated a decreasing trend. Notably, when the F/W molar ratio was larger than 0.4 in the precursor, the carrier mobility of the corresponding nanocrystals demonstrated a more sharper decreasing tendency than the that of the samples with F/W molar ratio below 0.4. The main scattering mechanism can be attributed to impurity doping. The higher F/W molar ratio in the precursor can cause the stronger scattering introduced by the dopant ions. On the other hand, the free carrier density firstly showed an increasing trend with the increase of F doping and reached 9.25 × 10^{14} cm^{-3} for 0.4-FCWO. After that, the free carrier density of 0.6-FCWO and 0.8-FCWO slightly decreased to 8.63 × 10^{14} cm^{-3} and 8.14 × 10^{14} cm^{-3}, respectively. The results can further explain the difference of absorption coefficient in Fig. 4. Specifically, 0.4-FCWO presented the best absorption coefficient in the wavelength starting from 780 nm to 2500 nm, which can be attributed to its high free carrier density shown in Table 2. High free carrier density can improve both of LSPR and small polaron transfer. Although the carrier mobility of 0.4-FCWO was lower than that of CWO, the absorption coefficient of 0.4-FCWO still demonstrated best optical performance. This is because the carrier mobility of 0.4-FCWO has not decreased too much and is close to the undoped sample. Besides, it can be obtained that the free carrier density has a dominant impact to determine the absorption coefficient than the carrier mobility.

Transmission electron microscopy was used to determine the TEM image, HR-TEM image, SAED pattern, and EDS pattern of 0.4-FCWO. The nanocrystals have a rod-like shape with a degree of agglomeration, as shown in Fig. 6a. The lattice spacing of 0.3840 nm and 0.6548 nm, which corresponds to the planes of (002) and (100), are shown in Fig. 6b. The SAED pattern in Fig. 6c confirmed the hexagonal structure of 0.4-FCWO. Figure 6d shows the element composition and shows the presence of the elements F, Cs, W, and O. The calculated Cs/W molar ratio is 0.31, which is quite close to the upper limit of 0.33 for Cs-HTBs. Besides, the calculated F/W molar ratio is 0.19, which is also close to the value measured by XPS.

To fabricate the 0.4-FCWO/PVA composite film, the as-synthesized 0.4-FCWO were mixed with PVA solution. Fig. 7 shows the spectra of ordinary glass without any coatings and the glass sample fabricated by the 0.4-FCWO/PVA dispersion. To evaluate the spectral selectivity of the glazing sample, four parameters were proposed, involving T_{Vis}, T_{NIR}, T_{lum}, and T_{sol} [33-35]. The corresponding values can be calculated by the following equations:

$$T_{\mathrm{vis}} = \frac{\int_{380}^{780} T\,(\lambda)d(\lambda)}{(780-380)\times 100} \times 100\% \quad (7)$$

$$T_{\mathrm{NIR}} = \frac{\int_{780}^{2500} T(\lambda)d(\lambda)}{(2500-780)\times 100} \times 100\% \quad (8)$$

$$T_{lum} = \frac{\int_{380}^{780} \varphi_{lum}(\lambda)T(\lambda)d(\lambda)}{\int_{380}^{780} \varphi_{lum}(\lambda)d(\lambda)} \times 100\% \quad (9)$$

$$T_{sol} = \frac{\int_{300}^{2500} \varphi_{sol}(\lambda)T(\lambda)d(\lambda)}{\int_{300}^{2500} \varphi_{sol}(\lambda)d(\lambda)} \times 100\% \quad (10)$$

Where $T(\lambda)$ indicates the measured transmittance spectra within a selected range, φ_{lum} represents standard luminous efficiency function for the photonic vision of human eyes and φ_{sol} implies solar radiation spectrum for air mass 1.5. Above calculated values are 67.21 %, 11.85 %, 72.76 % and 49.01 %, respectively. The composite film exhibits high visible light transmittance and near-infrared shielding performance in the glazing sample. The glazing sample with the composite coating has excellent spectral selectivity when compared to ordinary glass.

4. Conclusions

In this study, F-doped Cs_xWO_3 nanocrystals have been successfully synthesized to enhance the spectral tunability of LSPR and small polaron transfer by a controllable one-pot method. The phase components, element compositions, valence state of W ions and microstructure of the as-prepared nanocrystals were systematically examined. Moreover, the absorption coefficient spectra of the samples were calculated by the Beer-Lambert Law, and the free carrier density and carrier mobility were obtained by Hall effect measurement. This study is the first case in the literature interpreting the prospective connection between free carrier density/carrier mobility and optical performance in F-doped Cs_xWO_3 nanocrystals, indicating that aliovalent doping is an effective way to enhance spectral tunability. The results indicate that the free carrier density has a dominant impact to determine the absorption coefficient than the carrier mobility. When the F/W molar ratio is 0.4, the corresponding nanocrystals demonstrated best absorption property in the wavelength of near-infrared radiation. Furthermore, the transmittance spectra of the 0.4-FCWO/PVA composite film and the ordinary glass were also investigated. The composite film displayed excellent spectral selectivity with T_{Vis}, T_{NIR}, T_{lum}, and T_{sol} of 67.21 %, 11.85 %, 72.76 % and 49.01 %, respectively. This doping strategy provides promising potential to improve the spectral tunability for the practical application of energy-efficient windows.

Declaration of competing interest

The authors declare that they have no known competing financial interests or personal relationships that could have appeared to influence the work reported in this paper.

Acknowledgements

This work was supported by the TCS project of the Hong Kong Innovation and Technology Fund (UIT/139) and Sola Green Technologies Limited. This work was also supported by the National Natural Science Foundation of China (Grant No. 61705258).

References

[1] Yue X, Zhang T, Yang D, Qiu F, Wei G, Zhou H. Multifunctional Janus fibrous hybrid membranes with sandwich structure for on-demand personal thermal management. Nano Energy. 2019;63.

[2] Yue X, Chen H, Zhang T, Qiu Z, Qiu F, Yang D. Controllable fabrication of tendril-inspired hierarchical hybrid membrane for efficient recovering tellurium from photovoltaic waste. Journal of Cleaner Production. 2019;230:966-73.

[3] Wei G, Yang D, Zhang T, Yue X, Qiu F. Fabrication of multifunctional coating with high luminous transmittance, self-cleaning and radiative cooling performances for energy-efficient windows. Solar Energy Materials and Solar Cells. 2019;202.

[4] Wu X, Wang J, Zhang G, Katsumata K-i, Yanagisawa K, Sato T, et al. Series of MxWO3/ZnO (M = K, Rb, NH4) nanocomposites: Combination of energy saving and environmental decontamination functions. Applied Catalysis B: Environmental. 2017;201:128-36.

[5] Min Y, Chen Y, Yang H. Investigation on dynamic behaviour of condensation heat transfer in indirective evaporative cooler. Indoor and Built Environment. 2020.

[6] Zhou Y, Li N, Xin Y, Cao X, Ji S, Jin P. CsxWO3 nanoparticle-based organic polymer transparent foils: low haze, high near infrared-shielding ability and excellent photochromic stability. Journal of Materials Chemistry C. 2017;5:6251-8.

[7] Zeng X, Zhou Y, Ji S, Luo H, Yao H, Huang X, et al. The preparation of a high performance near-infrared shielding CsxWO3/SiO2composite resin coating and research on its optical stability under ultraviolet illumination. Journal of Materials Chemistry C. 2015;3:8050-60.

[8] Carboni M, Carravetta M, Zhang XL, Stulz E. Efficient NIR light blockage with matrix embedded silver nanoprism thin films for energy saving window coating. Journal of Materials Chemistry C. 2016;4:1584-8.

[9] Jelle BP, Kalnæs SE, Gao T. Low-emissivity materials for building applications: A state-of-the-art review and future research perspectives. Energy and Buildings. 2015;96:329-56.

[10] Hee WJ, Alghoul MA, Bakhtyar B, Elayeb O, Shameri MA, Alrubaih MS, et al. The role of window glazing on daylighting and energy saving in buildings. Renewable and Sustainable Energy Reviews. 2015;42:323-43.

[11] Garlisi C, Trepci E, Li X, Al Sakkaf R, Al-Ali K, Nogueira RP, et al. Multilayer thin film structures for multifunctional glass: Self-cleaning, antireflective and energy-saving properties. Applied Energy. 2020;264.

[12] Zheng L, Xiong T, Shah KW. Transparent nanomaterial-based solar cool coatings: Synthesis, morphologies and applications. Solar Energy. 2019;193:837-58.

[13] Shen B, Wang Y, Lu L, Yang H. Synthesis and characterization of Sb-doped SnO2 with high near-infrared shielding property for energy-efficient windows by a facile dual-titration co-precipitation method. Ceramics International. 2020;46:18518-25.

[14] Shen B, Wang Y, Lu L, Yang H. Spraying fabrication of spectrally selective coating with improved near-infrared shielding performance for energy-efficient glazing. Ceramics International. 2021;47:18991-7.

[15] Shen B, Wang Y, Lu L, Yang H. pH-dependent doping level and optical performance of antimony-doped tin oxide nanocrystals as nanofillers of spectrally selective coating for energy-efficient windows. Ceramics International. 2021;47:20335-40.

[16] Kang Y, Wu X, Gao Q. Plasmonic-Enhanced Near-Infrared Photocatalytic Activity of F-Doped (NH4)0.33WO3 Nanorods. ACS Sustainable Chemistry & Engineering. 2019;7:4210-9.

[17] Ran S, Liu J, Shi F, Fan C, Chen B, Zhang H, et al. Greatly improved heat-shielding performance of KxWO3 by trace Pt doping for energy-saving window glass applications. Solar Energy Materials and Solar Cells. 2018;174:342-50.

[18] Nakakura S, Arif AF, Machida K, Adachi K, Ogi T. Cationic Defect Engineering for Controlling the Infrared Absorption of Hexagonal Cesium Tungsten Bronze Nanoparticles. Inorg Chem. 2019;58:9101-7.

[19] Tandon B, Ghosh S, Milliron DJ. Dopant Selection Strategy for High-Quality Factor Localized Surface Plasmon Resonance from Doped Metal Oxide Nanocrystals. Chemistry of Materials. 2019;31:7752-60.

[20] Liu Z, Beaulac R. Nature of the Infrared Transition of Colloidal Indium Nitride Nanocrystals: Nonparabolicity Effects on the Plasmonic Behavior of Doped Semiconductor Nanomaterials. Chemistry of Materials. 2017;29:7507-14.

[21] Jansons AW, Koskela KM, Crockett BM, Hutchison JE. Transition Metal-Doped Metal Oxide Nanocrystals: Efficient Substitutional Doping through a Continuous Growth Process. Chemistry of Materials. 2017;29:8167-76.

[22] Diroll BT, Gordon TR, Gaulding EA, Klein DR, Paik T, Yun HJ, et al. Synthesis of N-Type Plasmonic Oxide Nanocrystals and the Optical and Electrical Characterization of their Transparent Conducting Films. Chemistry of Materials. 2014;26:4579-88.

[23] Buonsanti R, Milliron DJ. Chemistry of Doped Colloidal Nanocrystals. Chemistry of Materials. 2013;25:1305-17.

[24] Giannuzzi R, De Donato F, De Trizio L, Monteduro AG, Maruccio G, Scarfiello R, et al. Tunable Near-Infrared Localized Surface Plasmon Resonance of F, In-Codoped CdO Nanocrystals. ACS Appl Mater Interfaces. 2019;11:39921-9.

[25] Deokate RJ, Pawar SM, Moholkar AV, Sawant VS, Pawar CA, Bhosale CH, et al. Spray deposition of highly transparent fluorine doped cadmium oxide thin films. Applied Surface Science. 2008;254:2187-95.

[26] Santos- Cruz J, Torres- Delgado G, Castanedo- Perez R, Zúñiga- Romero CI, Zelaya- Angel O. Optical and electrical characterization of fluorine doped cadmium oxide thin films prepared by

the sol–gel method. Thin Solid Films. 2007;515:5381-5.

[27] Cho SH, Ghosh S, Berkson ZJ, Hachtel JA, Shi J, Zhao X, et al. Syntheses of Colloidal F:In2O3 Cubes: Fluorine-Induced Faceting and Infrared Plasmonic Response. Chemistry of Materials. 2019;31:2661-76.

[28] Swallow JEN, Williamson BAD, Whittles TJ, Birkett M, Featherstone TJ, Peng N, et al. Self-Compensation in Transparent Conducting F-Doped SnO2. Advanced Functional Materials. 2018;28.

[29] Nadarajah A, Carnes ME, Kast MG, Johnson DW, Boettcher SW. Aqueous Solution Processing of F-Doped SnO2 Transparent Conducting Oxide Films Using a Reactive Tin(II) Hydroxide Nitrate Nanoscale Cluster. Chemistry of Materials. 2013;25:4080-7.

[30] Song X, Liu J, Shi F, Fan C, Ran S, Zhang H, et al. Facile fabrication of KmCsnWO3 with greatly improved near-infrared shielding efficiency based on W5+-induced small polaron and local surface plasmon resonance (LSPR) modulation. Solar Energy Materials and Solar Cells. 2020;218.

[31] Pasquarelli RM, Ginley DS, O'Hayre R. Solution processing of transparent conductors: from flask to film. Chem Soc Rev. 2011;40:5406-41.

[32] Staller CM, Gibbs SL, Saez Cabezas CA, Milliron DJ. Quantitative Analysis of Extinction Coefficients of Tin-Doped Indium Oxide Nanocrystal Ensembles. Nano Lett. 2019;19:8149-54.

[33] Cai L, Wu X, Gao Q, Fan Y. Effect of morphology on the near infrared shielding property and thermal performance of K0.3WO3 blue pigments for smart window applications. Dyes and Pigments. 2018;156:33-8.

[34] Zhao Z, Bai Y, Ning W, Fan J, Gu Z, Chang H, et al. Effect of surfactants on the performance of 3D morphology W18O49 by solvothermal synthesis. Applied Surface Science. 2019;471:537-44.

[35] Li X-H, Liu C, Feng S-P, Fang NX. Broadband Light Management with Thermochromic

Hydrogel Microparticles for Smart Windows. Joule. 2019;3:290-302.

Table 1 The molar ratio of Cs/W and F/W in nanocrystal samples measured by XPS

Sample	Cs/W molar ratio	F/W molar ratio
CWO	0.31	0
0.2-FCWO	0.18	0.14
0.4-FCWO	0.30	0.21
0.6-FCWO	0.27	0.23
0.8-FCWO	0.25	0.24

Table 2 The free carrier density and carrier mobility of as-prepared F-doped Cs_xWO_3 samples

Sample	Free carrier density (cm^{-3})	Carrier mobility ($cm^2\ V^{-1}\ s^{-1}$)
CWO	5.83×10^{14}	16.62
0.2-FCWO	6.41×10^{14}	15.71
0.4-FCWO	9.25×10^{14}	14.83
0.6-FCWO	8.63×10^{14}	12.35
0.8-FCWO	8.14×10^{14}	10.62

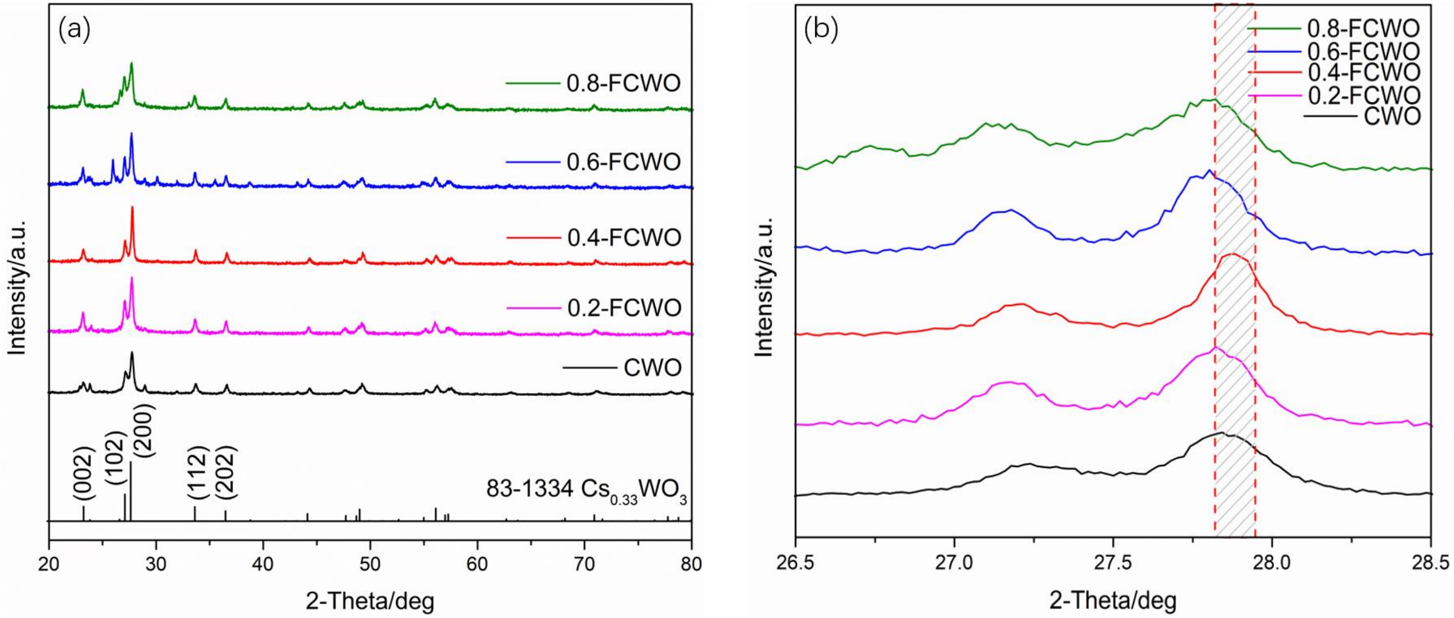

Fig. 1 (a) XRD pattens, (b) high-resolution patterns corresponding to crystal plane (102) and (200) of CWO, 0.2-FCWO, 0.4-FCWO, 0.6-FCWO and 0.8-FCWO.

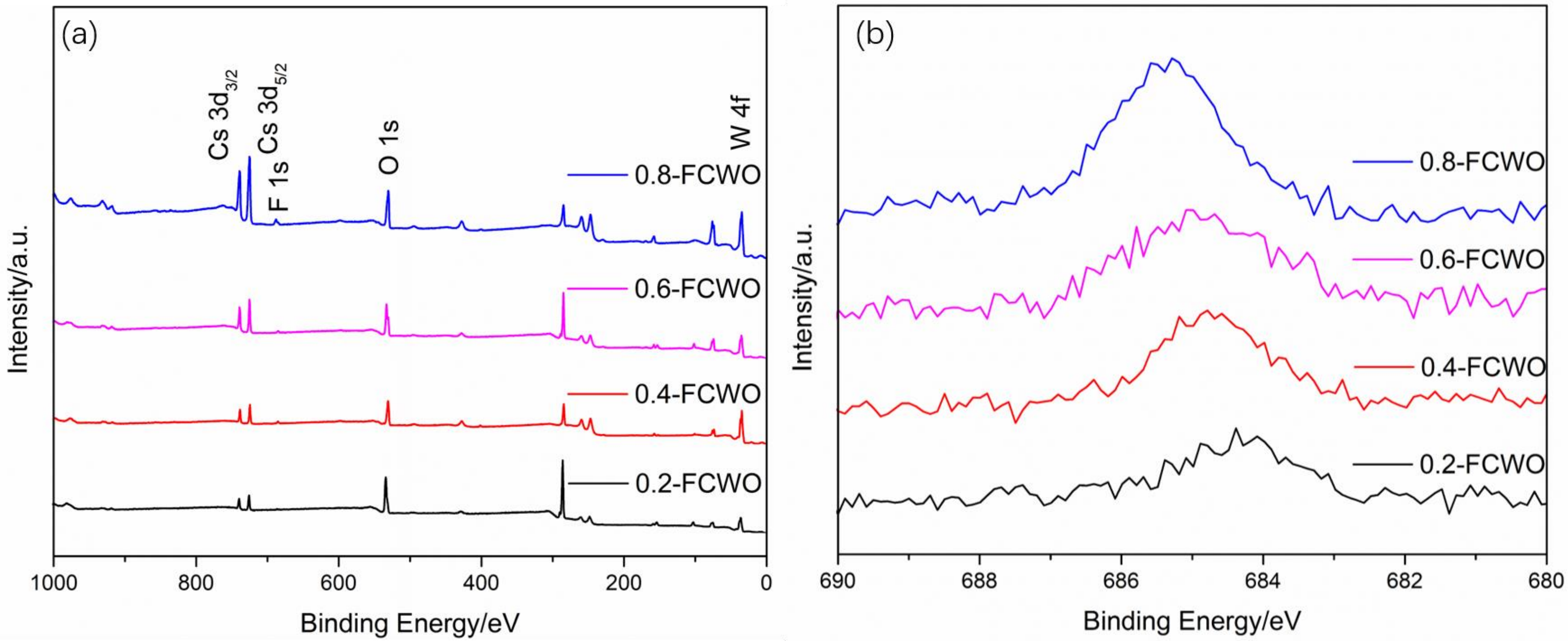

Fig. 2 (a) The survey spectra and (b) the F 1s core-level spectra of 0.2-FCWO, 0.4-FCWO, 0.6-FCWO and 0.8-FCWO.

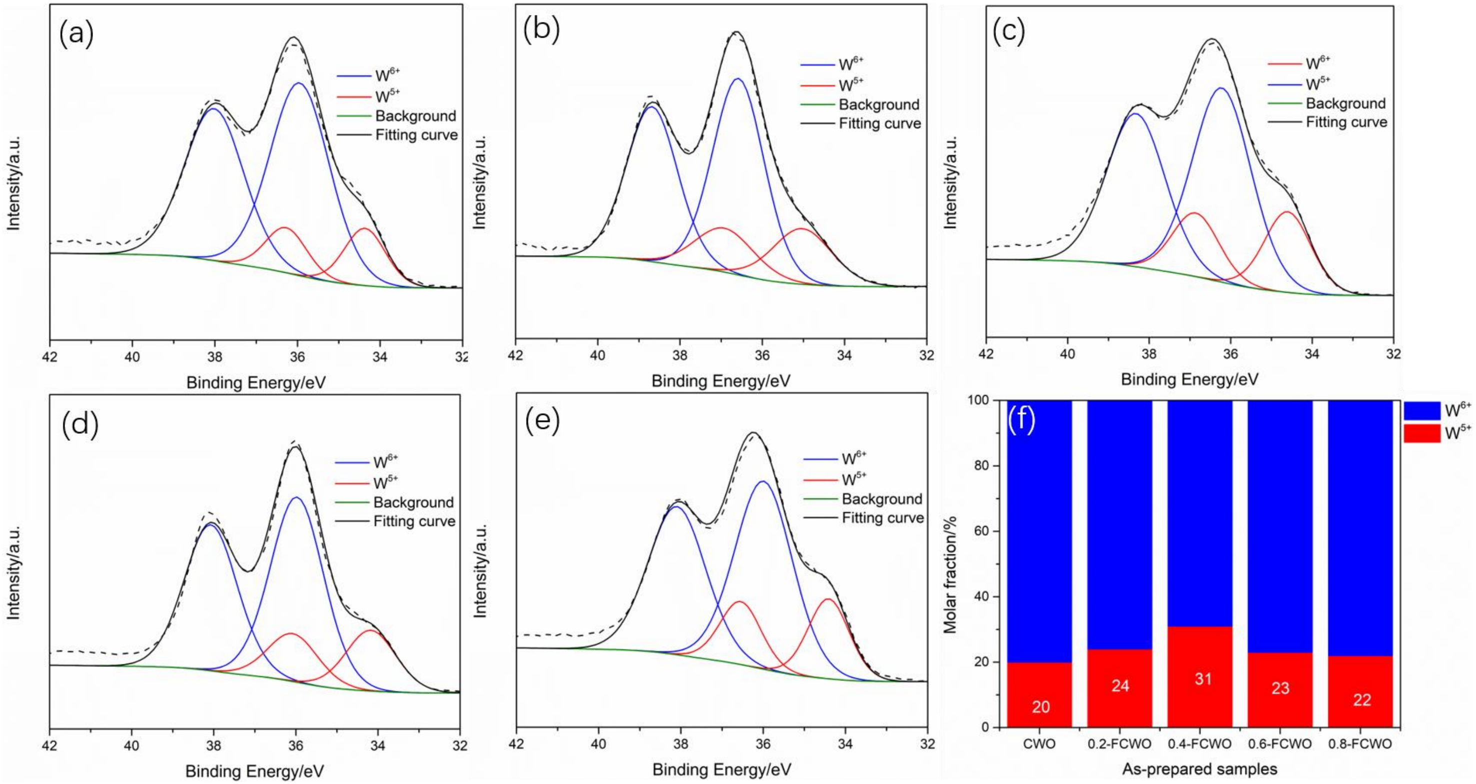

Fig. 3 The W4f core-level spectra of (a) CWO, (b) 0.2-FCWO, (c) 0.4-FCWO, (d) 0.6-FCWO, (e) 0.8-FCWO; (d) The valence distribution of W element in CWO, 0.2-FCWO, 0.4-FCWO, 0.6-FCWO and 0.8-FCWO.

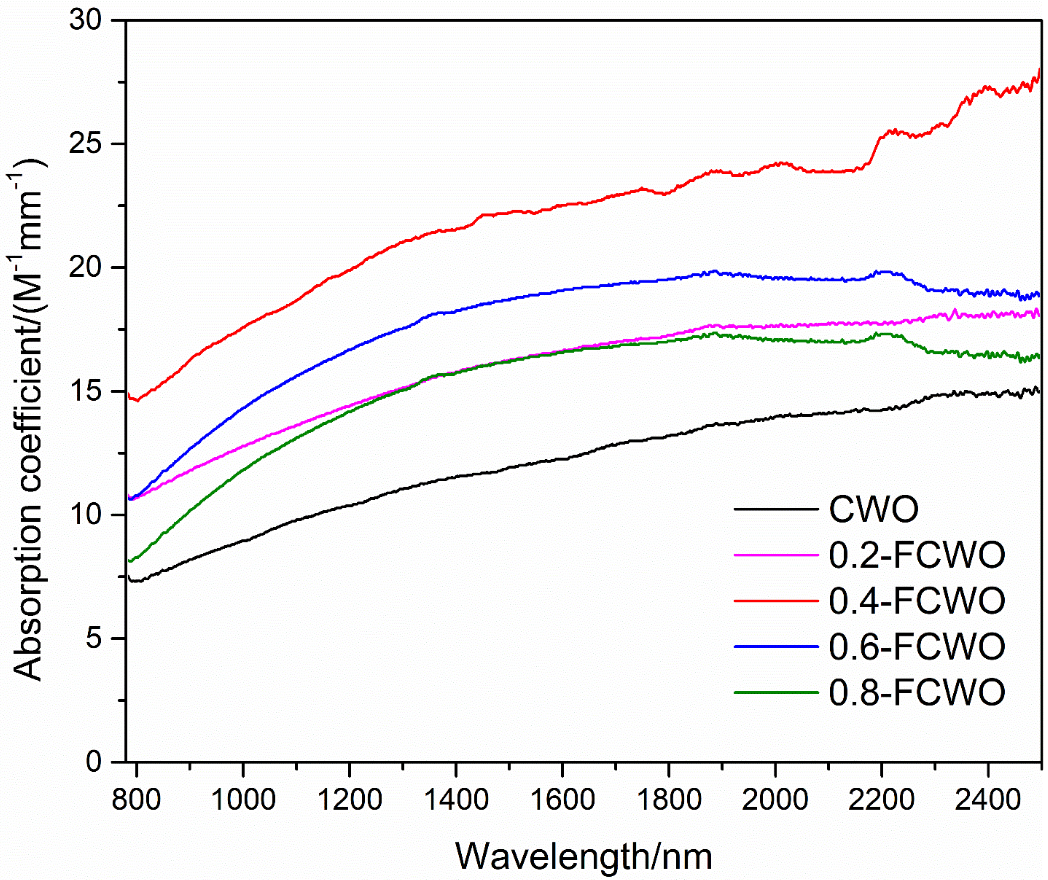

Fig. 4 The absorption coefficient spectra of CWO, 0.2-FCWO, 0.4-FCWO, 0.6-FCWO and 0.8-FCWO.

Figure 5

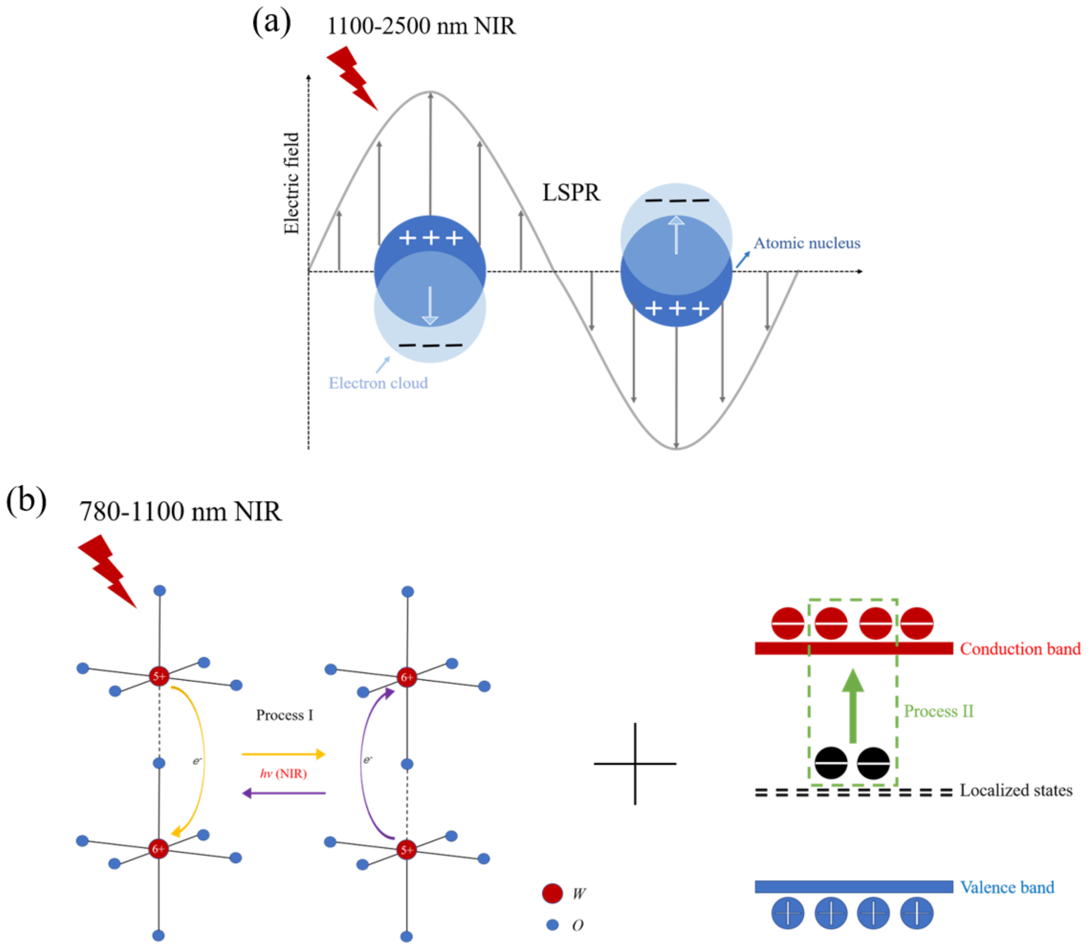

Fig. 5 The schematic diagram of (a) LSPR under 1100-2500 nm NIR and (b) small polaron transfer under 780-1100 nm NIR.

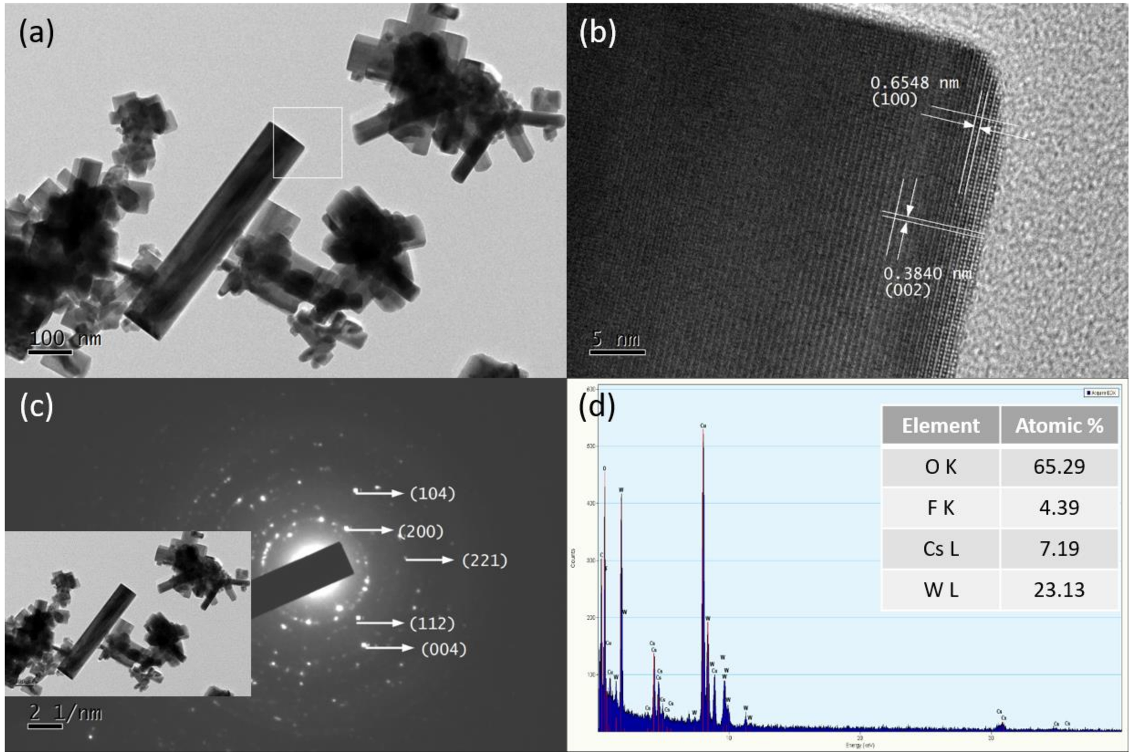

Element	Atomic %
O K	65.29
F K	4.39
Cs L	7.19
W L	23.13

Fig. 6 (a) TEM image, (b) HR-TEM image, (c) SAED pattern and (d) EDS pattern of 0.4-FCWO.

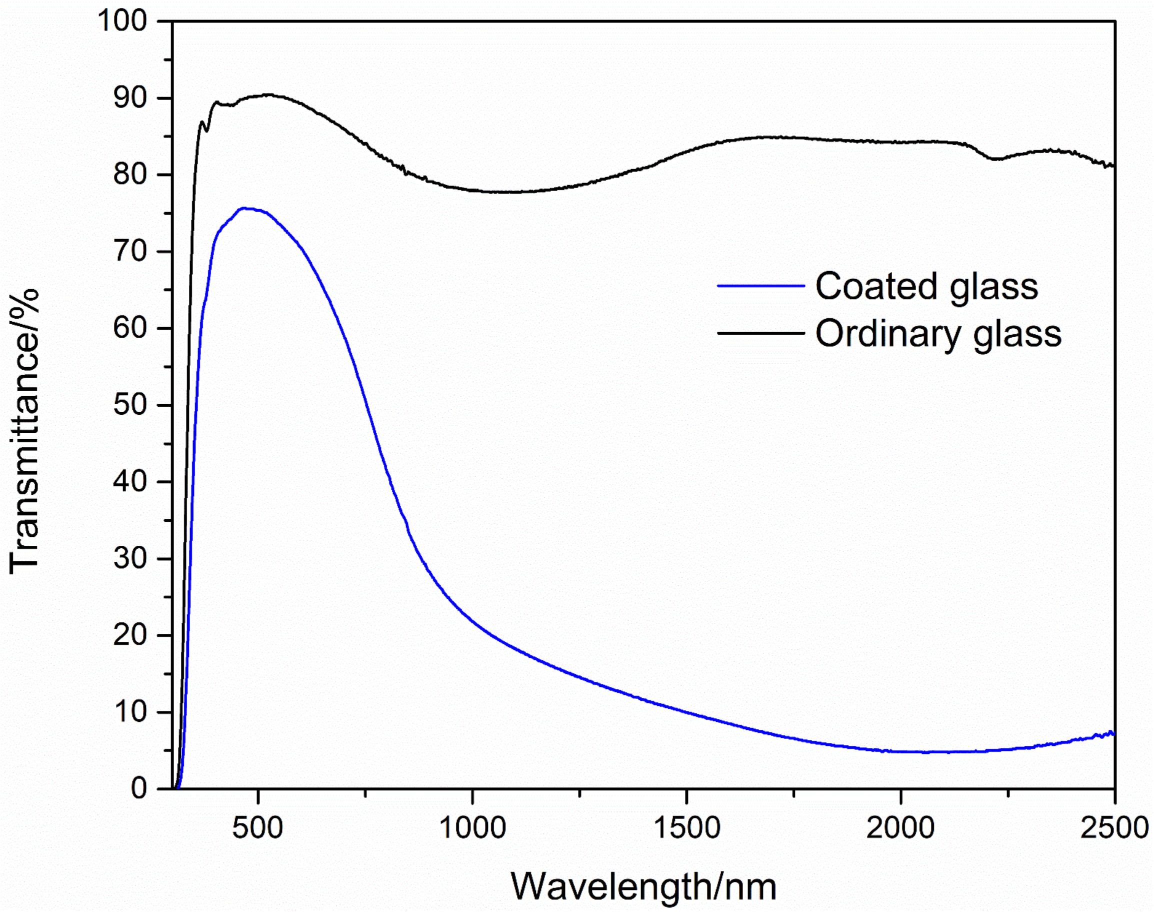

Fig. 7 The transmittance spectra of the coated glass with the 0.4-FCWO/PVA composite film and the ordinary glass.